OPEN ACCESS
IOP Publishing
Classical and Quantum Gravity
Class. Quantum Grav. **42** (2025) 225025 (20pp)
https://doi.org/10.1088/1361-6382/ae1c15

Simulation of UV light propagation in the LISA charge management system fiber optics

Corey J Richardson*, **Simon Barke, Brij Patel, Lea Bischof, Stephen Apple, Peter J Wass and John W Conklin**

University of Florida, Gainesville, FL, United States of America

E-mail: corey.richardson@ufl.edu

Received 20 June 2025; revised 8 October 2025
Accepted for publication 5 November 2025
Published 21 November 2025

Abstract

A ray model has been developed to characterize how a new, redundant fiber optic harness (FOH) design affects the UV light propagation in the Laser Interferometer Space Antenna (LISA) charge management system. LISA will be the first gravitational wave (GW) observatory in space, detecting GWs in the 0.1 mHz–1 Hz range. The endpoint of each LISA interferometer arm is a free-falling test mass (TM), which accumulates charge from cosmic rays over time and leads to force noise in GW measurements. LISA will utilize photoelectric discharge via UV light to control the TM charge, which was successfully demonstrated on LISA Pathfinder (LPF). The delivery of UV light on LISA differs from LPF's design by using UV LEDs, rather than Hg lamps, and a novel, redundant multicore FOH, which has four different configurations. The FOH light output is injected into an optical feedthrough (OFT), which injects the light into the TM housing. In MATLAB, a Gaussian model of the FOH light output was developed for each configuration and used to generate a ray distribution of each FOH light output. This ray model was propagated through the geometry of the OFT in COMSOL Multiphysics to simulate the final ray distribution that will be used in future simulations. The simulated power and beam divergence of the ray model is consistent with experimental values for each FOH configuration to 8%. The ray model accurately characterizes the

* Author to whom any correspondence should be addressed.

difference in each FOH configuration such that the effects of the redundant LISA FOH design can be further investigated with a photoelectric charge management simulation of the LISA UV discharge process.

Keywords: LISA, gravitational wave detection, UV discharge, fiber optics, ray tracing

1. Introduction

Gravitational waves (GWs)—ripples in spacetime caused by highly energetic events in our Universe—are a key to understanding the dark cosmos and the nature of gravity. Their first direct observation came in 2015, when LIGO [1] detected GWs from the merger of two stellar-mass black holes, confirming the existence of GWs and further solidifying general relativity. LIGO, along with Virgo [2], is a ground-based interferometric GW observatory operating in the 10 Hz–10 kHz frequency range, allowing detection of GWs from stellar-mass black hole binaries, neutron star binaries, and supernovae. Seismic noise, however, imposes a low-frequency limit at $\sim$10 Hz, preventing ground-based observatories from detecting lower-frequency GWs such as those from supermassive black hole binaries and extreme mass ratio inspirals.

The Laser Interferometer Space Antenna (LISA) [3] will be the first GW observatory in space, eliminating the seismic noise limitation of ground-based detectors. LISA will operate in the 0.1 mHz to 1.0 Hz frequency range, broadening our view of the gravitational Universe in concert with LIGO and Virgo. As a joint mission between the European Space Agency (ESA) and the National Aeronautics and Space Administration (NASA), LISA was formally adopted by ESA in 2024 and is scheduled to launch in 2035 with a nominal science mission duration of 4.5 years. The LISA constellation will consist of three identical drag-free spacecraft orbiting the Sun in a near-equilateral triangle formation with 2.5×10^6 km interferometer arms. Each of the three spacecraft will house two test masses (TMs), which serve as end mirrors for the three laser interferometer arms. The fundamental measurement of LISA is the differential change in the distance between TMs in separate spacecraft—i.e. the changing length of an interferometer arm—caused by passing GWs. The LISA spacecraft will utilize drag-free control to ensure the TMs follow pure geodesic trajectories, isolating them from non-gravitational forces and allowing high-precision GW detection. Each TM is housed in a gravitational reference sensor (GRS), which shields the TM from external forces and actively maintains the necessary geodesic trajectory for each spacecraft [4].

1.1. LISA GRS

The GRS is composed of the TM and its housing, which is lined with electrodes for capacitive sensing and electrostatic actuation of the TM position and orientation along with measurement of the TM charge. The GRS is contained in a vacuum enclosure and keeps the TM isolated from exterior non-gravitational forces. The TM is a 2 kg Au–Pt (70/30) alloy cube measuring 46 mm on each side and coated in gold. The Au–Pt alloy was chosen for its low magnetic susceptibility and high density, while the gold coating provides a reflective and electrostatically homogeneous surface [4]. A total of 18 electrodes line the interior surface of the housing, six of which are used to apply a 4.9 V AC injection signal at 98 kHz to induce a 0.6 V potential on the TM. This potential allows the remaining 12 electrodes (two per cube face) to perform capacitive sensing at 98 kHz and actuation at audio frequencies of the TM position with 6 degrees of freedom [4].

Despite shielding from external forces, stray accelerations in the measurement frequency range of 0.1 mHz–1.0 Hz persist. Thus, a requirement is imposed on the allowable TM acceleration noise level in the LISA frequency range, of which the minimum is $3 \times 10^{-15}\,\mathrm{m\,s^{-2}\,Hz^{-1/2}}$ at 1 Hz. In the mHz range of the LISA frequency band, the dominant noise source is TM charging due to incident cosmic rays, charged particles that cause the TM to accumulate a net charge [4]. Residual electric fields and fluctuations produced by the spacecraft electronics interact with the charged TM and its fluctuations, inducing a Coulomb force, $\overrightarrow{F} = q\overrightarrow{E}$, on the TM [5]. The two dominant electrostatic noise sources are the DC electric field interaction with TM charge fluctuations and DC TM charge interaction with electric field fluctuations.

The GRS shields the TM from most charged particles, but particles with energies > 100 MeV (mostly protons and He-4 nuclei) can penetrate the shielding and land on the TM [6, 7]. The LISA requirement for the maximum allowable net TM charge is 2.4 pC, or 1.5×10^7 e [7]. This corresponds to a TM potential of ± 70 mV, at which point the Coulomb force on the TM exceeds the LISA acceleration noise requirement. At predicted TM charging rates of 20–49 $\mathrm{e\,s^{-1}}$ [8], the TM charge could exceed requirements in just a few days. To control the TM charge over time and maintain noise levels within the LISA requirement, a charge management system (CMS) is implemented.

1.2. LISA CMS

Charging of free-falling TMs in space is not a new problem; past missions such as CHAMP [9] and GRACE [10]/GRACE Follow-On [11], which measured the Earth's magnetic geopotential and gravity field, respectively, used μm-diameter gold and platinum grounding wires to remove TM charge. Due to the acceleration noise requirement for LISA, grounding-wire discharge is not feasible. LISA will build on Gravity Probe B (GP-B) [12] heritage, which first performed contactless discharge via the photoelectric effect. By illuminating the TM or electrode housing with UV light, electrons are emitted from the respective surface without the noise associated with grounding wire contact.

The LISA CMS will use UV discharge to meet the TM charge requirement. Within the GRS, the gold-coated TM and electrode housing have a work function of 4.1–4.9 eV (4.1–4.3 eV per [13] and 4.3–4.9 per [14]), which requires light with a maximum wavelength of $\sim$250–300 nm for photoelectron emission. This places the required wavelengths for LISA TM discharging in the deep UV range ($\lambda < 280$ nm). Deep UV LEDs with a 250 nm average peak wavelength have been chosen as the UV source for LISA and have been extensively tested for performance and reliability at the University of Florida (UF) [15] and reproducibility and stability on ground and in space by Stanford University [16].

The LISA CMS, of which there is one on each spacecraft, is composed of the charge management device (CMD), OFT, GRS head, and front-end electronics. The CMD is being developed by the Precision Space Systems Lab at UF and consists of two components: the UV light unit (ULU) and fiber optic harness (FOH) [17].

The LISA spacecraft will each contain a main and redundant ULU, each of which feeds UV light to both GRS heads onboard via the FOH. Each ULU contains a power source, current driver, necessary electronics, and 12 UV LEDs housed within two opto-mechanical assemblies (OMAs), with six LEDs in each for internal redundancy. The FOH directs light from four separate LEDs, from separate OMAs on each ULU, to an OFT located at one of the three GRS injection ports. The OFT injects UV light from the FOH though the vacuum enclosure and into the GRS. Depending on the injection port, light is directed onto either the TM or

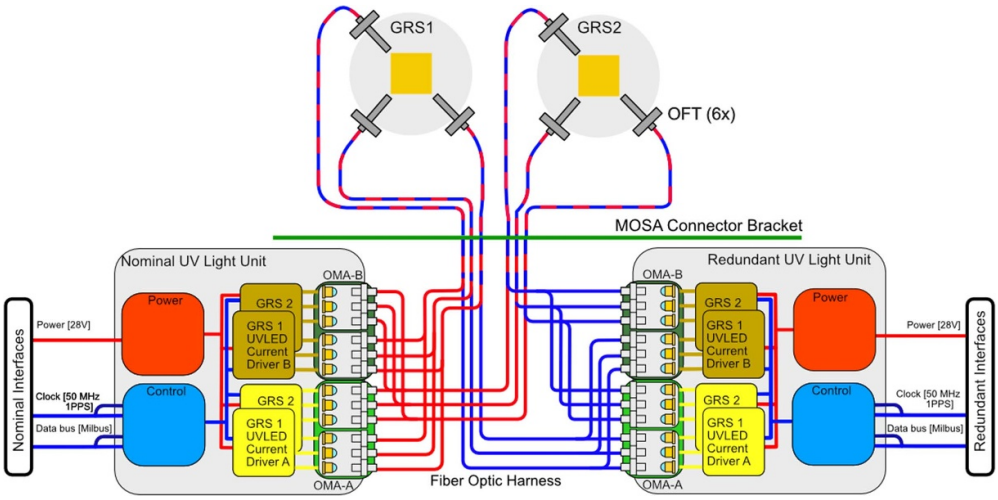

Figure 1. Block diagram of the LISA CMD within one LISA spacecraft. The FOH redundancy is shown by the red and blue paths leading from four LEDs to one OFT. The nominal and redundant ULUs are shown with additional internal redundancy for the current drivers and OMAs via A and B designations. Note how one FOH guides light from an LED in each of the four OMAs to one single OFT, providing multiple levels of redundancy.

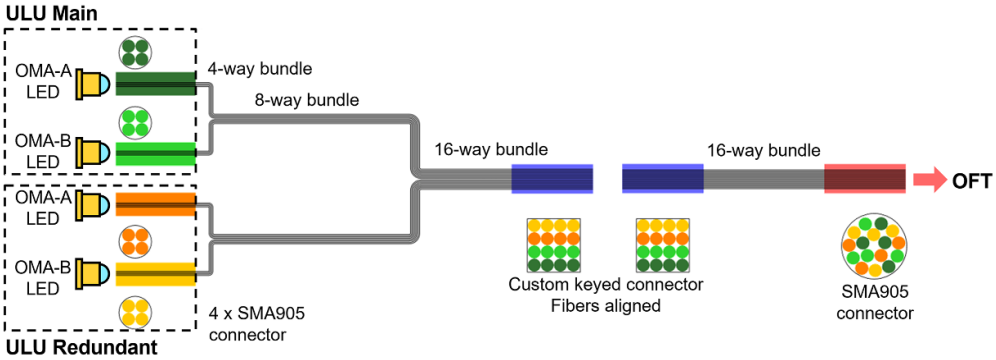

Figure 2. Diagram of FOH path from input (LEDs coupled to four 4-core fibers on the left) to output (16-core fiber coupled to OFT on the right). Core pattern shown (16-core bundle on the right) is representative of randomized core pattern concept, not of the FOH prototype used for testing.

electrode housing, allowing bidirectional control of electron flow within the GRS. The redundancy scheme for the LISA CMD is shown in figures 1 and 2.

1.3. LISA fiber optics

Each spacecraft will contain six FOHs, one for each injection port on each GRS. The FOH, shown in figures 2 and 3(a), is a multicore optical fiber, measuring $\sim$2 m in length, that merges the input of four 4-core fibers into a single 16-core fiber end that couples to the OFT. Each core is an individual 200 μm-diameter silica multimode fiber. The LISA FOH design incorporates

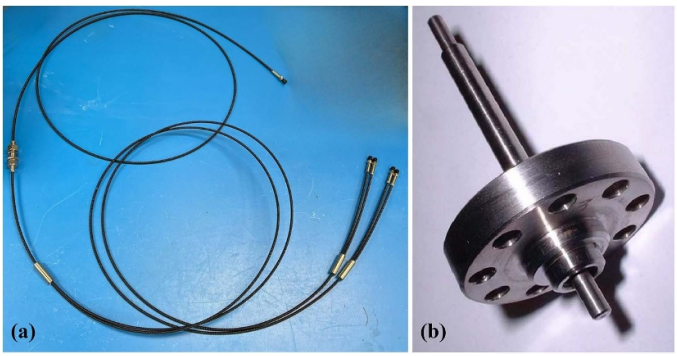

Figure 3. (a) LISA FOH Prototype. (b) LISA Pathfinder ISUK (nearly identical to LISA OFT) Reproduced with permission from [18].

redundancy, delivering light from the main and redundant ULUs to each injection port. Each grouping of four cores that couples to one LED is called a leg, such that there are four legs per FOH. The core locations in the output end of the FOH are not specified or controlled during manufacturing, resulting in a randomized light output pattern for each leg. Across the LISA mission, there are 72 FOH legs with potentially distinct light outputs. The general concept of the randomized core patterns in the FOH output is shown in figure 2.

The FOH output is coupled to the OFT, which injects the UV light into the vacuum enclosure of the GRS. The OFT (formerly known as the Inertial Sensor UV Kit (ISUK) on LISA Pathfinder (LPF)) is a simple silica optical fiber, with a core 1 mm in diameter and 67.3 mm in length, contained in a titanium vacuum feedthrough. The OFT channels the light to its respective injection port, circularizing the asymmetric FOH light output in the process. The OFT core is pure silica with a refractive index of 1.504 and the cladding is F-doped silica with a refractive index of 1.488, giving a numerical aperture of 0.219 and expected maximum acceptance angle of 12.6°. The UV light beam profile exiting the OFT is dependent on the FOH configuration—which leg is active and, consequently, which four cores are illuminated. Illuminated cores in the periphery of the FOH output produce more skew ray propagation in the OFT, while central cores produce more meridional rays [19]. This leads to significantly different light outputs from the OFT depending on the FOH configuration, which is further discussed in section 4.

1.4. LPF

LPF [20] was a technology demonstration mission for LISA that launched to an Earth-Sun L1 orbit in 2015. LPF carried two LISA-like GRS subsystems with laser interferometers to measure the positions of the two free-falling TMs. A key objective of LPF was measuring the stray non-gravitational acceleration noise on the TMs, which were discharged using UV light. LPF had an acceleration noise requirement of $3 \times 10^{-14}\,\mathrm{m\,s^{-2}\,Hz^{-1/2}}$ at 1 mHz, one order of magnitude higher than that of LISA. After 16 months of operation, LPF demonstrated stray acceleration noise levels meeting both its own requirement and the LISA requirement [20].

The LPF CMS used the same basic design as LISA, but lacked redundancy and differed in UV light source and FOH design. Like GP-B before, LPF used mercury lamps as a UV light source for TM discharge [21]. The LPF FOH was a 19-core multimode fiber, consisting of the same 200 μm cores, where each injection port only received light from a single mercury lamp [22]. The 19 cores in each FOH ran from the input to the output; there were no separate

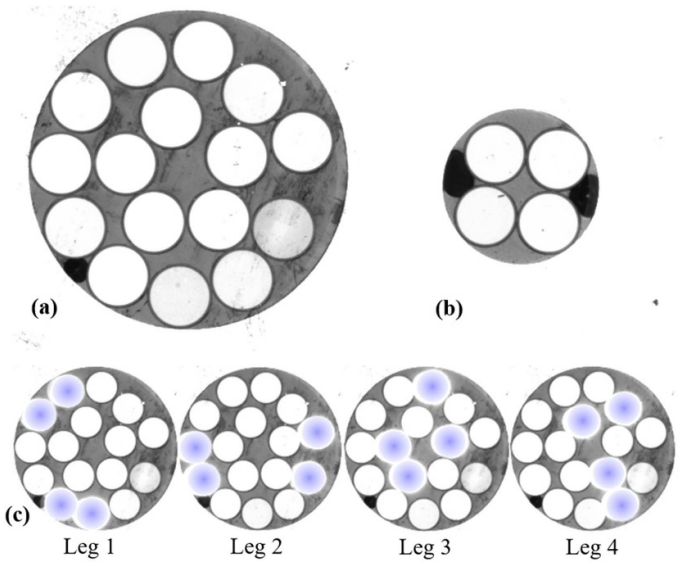

Figure 4. (a) 16-core output end of the LISA FOH prototype (1.0 mm diameter). (b) 4-core input end of one LISA FOH prototype leg (0.6 mm diameter). (c) Core illumination patterns for each leg (configuration) of the LISA FOH prototype.

legs and thus no redundancy beyond the three UV injection ports per GRS. Each LPF FOH produced a near-Gaussian output, differing in light cone half angles but providing consistent UV beam profile shapes across all injection ports [18]. The proposed LISA OFT is ∼8 mm shorter, yet otherwise the same as the LPF ISUK.

1.5. Motivation for FOH study

The success of the LPF CMS necessitates validation of the design modifications for the LISA CMS. A photoelectric charge management simulation is being developed at UF to simulate the UV discharge process and investigate how design changes affect the efficacy of the LISA CMD. The simulation, which will be described in detail in a future publication, uses the GRS geometry and modeled OFT light output to calculate photon trajectories and reflections in the GRS and resultant surface electron emissions. A key objective of this simulation is to determine how the apparent yield—defined as the number of electrons emitted per injected photon, a key measure of UV discharge efficiency—varies with the FOH configuration. Depending on the core locations within an FOH configuration (see figure 4), the photon topography within the UV light beam will change. If the photons are too concentrated in the middle of the beam, i.e. the beam is too narrow, the light may not achieve the needed illumination spread within the GRS and the CMD may not perform to the standard set by LPF.

Since the UV light output of the OFT is an input to the photoelectric charge management simulation, a model of the OFT output for each FOH leg configuration must first be developed. This paper presents a model of the FOH light output for each leg and a simulation of its propagation through the OFT geometry to obtain a ray model of the OFT light output. The ray model is used to characterize the OFT light output, providing the ray direction vectors required as input for the photoelectric charge management simulation.

Additionally, ESA is currently in the process of defining requirements for the FOH-OFT coupling interface. A model that accurately characterizes the FOH light output with respect to LPF results will aid in developing these requirements.

2. FOH/OFT interface characterization and model

To develop a final ray model of the OFT beam profile, the light output of the FOH and its propagation through the OFT are both simulated. The FOH output model is derived by fitting Gaussian parameters to image data and is used to generate a ray distribution for each FOH leg. This ray distribution is input into a geometrical optics simulation of the OFT to model the light propagation in the OFT and output beam profile. The ray trajectories representing the OFT light output serve as the input to the photoelectric charge management simulation. The following subsections detail the FOH output model development, followed by the OFT geometrical optics simulation in section 3.

The first step in developing a model for the light output of each FOH leg is imaging the beam as it propagates away from the FOH output end. Beam imaging enables initial qualitative characterization and development of mathematical expressions for each of the beam's features.

2.1. Experimental characterization of FOH light output

To characterize the FOH output for each leg, the measurement setup shown in figure 5 was used to take successive images of the light exiting an FOH prototype (seen in figure 3) at multiple distances. The 4-core input end of the FOH was coupled to an assembly replicating the designed separation of the UV LED and the FOH input fiber tip, such that the LED beam waist is focused into the fiber. The LED was driven at a constant 20 mA current for all measurements, and the power output of the LED and each FOH leg were measured with a Thorlabs PM100D power meter and S120VC photodiode with SMA fiber adapters. Power measurements allow normalized intensity values from each image to be scaled and directly compared.

The output end of the FOH was directed into a custom-made DataRay WinCamD-LCM beam imaging camera (WinCam), mounted on a Thorlabs MTS50-Z8 linear translation stage to allow imaging of the light profile at different distances. The FOH fiber tip itself was secured in a custom mount that aligned the FOH tip with the 11.3 mm $\times$ 11.3 mm square WinCam lens. To ensure that systematic errors were not present in the measurements, an evaluation of the WinCam-FOH alignment was performed by rotating the FOH tip and measuring the launch angle at each rotation angle. Alignment accuracy within $\pm 0.32^{\circ}$ was demonstrated based on the standard deviation of the measured FOH launch angles. The WinCam, linear translation stage, and source measure unit driving the LED were all controlled via LabView to take 51 images of the FOH prototype output for each leg. The 51 WinCam images were taken at equidistant steps between 1.3 mm and 6.3 mm from the FOH tip (every 0.1 mm), where 1.3 mm is the closest possible distance between the WinCam and FOH tip without risk of damaging components. The WinCam output is a 1280 $\times$ 1280 matrix of relative intensity values recorded on a 16-bit scale (0 to $2^{16} - 1$). An example of the WinCam images for leg 1 of the FOH prototype are shown in figure 6. By imaging the FOH beam at successive distances, the propagation behavior can be observed and modeled.

In the WinCam images for each leg, a peak in intensity at each illuminated core is observed. Each peak is accompanied by a ring of elevated intensity believed to arise from a cladding mode, where light enters the fiber cladding and exits the cladding in a dull ring of light. The ring can best be seen in the 2.3 mm image in figure 6. The beam profile for each core is modeled as

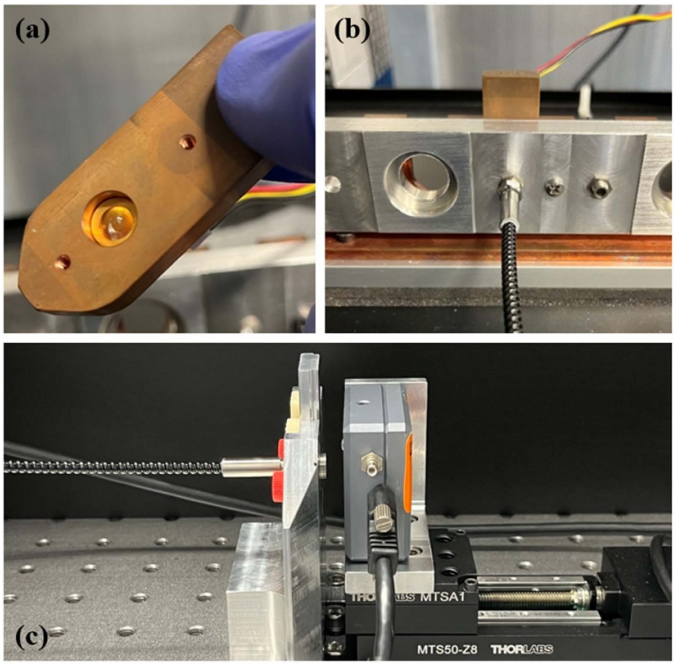

Figure 5. Experimental setup for imaging FOH beam profile. (a) LED ball lens assembly mounted in copper block. (b) Copper block mounted in a bracket allowing for FOH coupling, with LED connected to power source. (c) FOH output end directed into the WinCam, which is mounted on the linear translation stage.

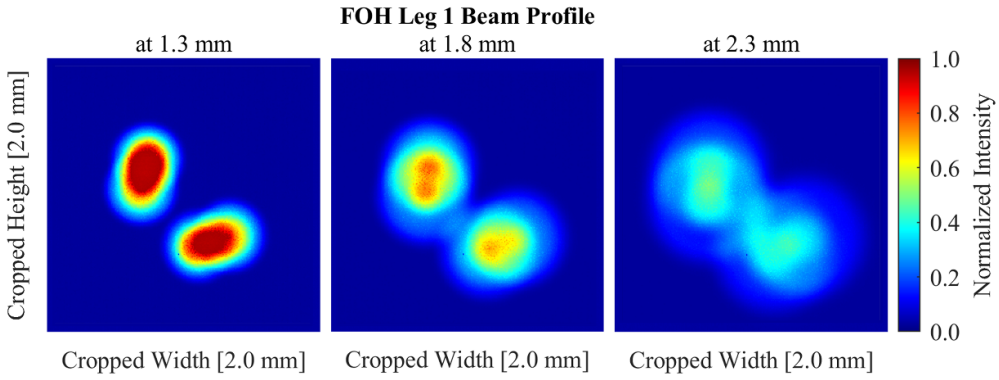

Figure 6. WinCam images of FOH prototype leg 1, taken 1.3 mm, 1.8 mm, and 2.3 mm from the FOH tip. The intensity scale is normalized to the maximum WinCam output of $2^{16} - 1$. The core layout for leg 1 can be seen in figure 4, where the cores are clustered in two groups of two. The WinCam images here are rotated slightly counterclockwise relative to the FOH output images in figure 4.

the sum of a Gaussian distribution and Gaussian ring distribution, which is a circular intensity profile formed by sweeping a 2-dimensional Gaussian distribution along the circumference of a circle.

2.2. Gaussian best-fit model

For each FOH prototype leg, the light output was modeled with a Gaussian distribution and a Gaussian ring distribution centered at each illuminated core. To find the Gaussian parameters that govern the beam propagation, each WinCam image was fit to a sum of four two-dimensional Gaussian distributions and four two-dimensional Gaussian ring distributions, where

$$f_{\mathrm{G}}\left(x,y,a_{\mathrm{G}},\sigma_{\mathrm{G}}\right)=a_{\mathrm{G}}\mathrm{e}^{-\left[(X-x)^2+(Y-y)^2\right]/\left(2\sigma_{\mathrm{G}}^2\right)} \tag{1}$$

defines an individual Gaussian profile exiting one of the illuminated cores, and

$$f_{\mathrm{R}}\left(x,y,a_{\mathrm{R}},\sigma_{\mathrm{R}},R\right)=a_{\mathrm{R}}\mathrm{e}^{-\left[\sqrt{(X-x)^2+(Y-y)^2}-R\right]^2/\left(2\sigma_{\mathrm{R}}^2\right)} \tag{2}$$

defines an individual Gaussian ring profile. The parameters are the pixel location of the core center, $[x,y]$, the main and ring Gaussian amplitudes, a_{G} and a_{R}, the standard deviations, σ_{G} and σ_{R}, and the radius of the Gaussian ring, R. The pixel mesh elements are represented by X and Y, spanning 1–1280. Summing equations (1) and (2) gives the equation for the light exiting a single core,

$$f_{core}\left(x,y,a_{\mathrm{G}},a_{\mathrm{R}},\sigma_{\mathrm{G}},\sigma_{\mathrm{R}},R\right)=f_{\mathrm{g}}\left(x,y,a_{\mathrm{G}},\sigma_{\mathrm{G}}\right)+f_{r}\left(x,y,a_{\mathrm{R}},\sigma_{\mathrm{R}},R\right), \tag{3}$$

as a function of all seven parameters. The equation for the entire light output from the four illuminated cores of one FOH leg is given by,

$$f_{\mathrm{beam}}=\sum_{i=1}^{4}f_{\mathrm{core},i}+I_{\mathrm{bg}} \tag{4}$$

where I_{bg} is the mean background noise intensity. To model the FOH output for a given leg, equation (4) was fit to each of the 51 WinCam images by minimizing the cost function,

$$J=\sum_{X=1}^{1280}\sum_{Y=1}^{1280}\left(f_{\mathrm{beam}}\left(X,Y\right)-W(X,Y)\right)^2 \tag{5}$$

where W is the WinCam matrix of intensity values at a given distance. Equation (5) was minimized using MATLAB's `fminsearch`, which outputs the seven best-fit parameters for each core and the mean background noise intensity, giving 29 best-fit parameters for a specified WinCam image. The 29 parameters were found for all 51 images of each FOH leg's light output.

By plotting each parameter against the respective image's distance from the FOH tip, the propagation behavior was observed and modeled with a least-squares optimization. In order to generate a ray distribution that represents the FOH light output, only five of the parameters for each core are needed: x, y, σ_{G}, σ_{R}, and R. The Gaussian amplitudes, a_{G} and a_{R}, and the background noise, I_{bg}, are needed to fit equation (4) to the WinCam data, but they serve no purpose in generating the ray distributions, as the intensity is reflected by the number of rays per unit area. The standard deviations σ_{G} and σ_{R} are analogous to the beam width, which does not diverge perfectly linearly for Gaussian beams. The beam's local divergence angle is small or negative near the waist (near-field) and asymptotically approaches the beam's far-field divergence angle with increasing distance [23]. For this model, a linear fit was found for the standard

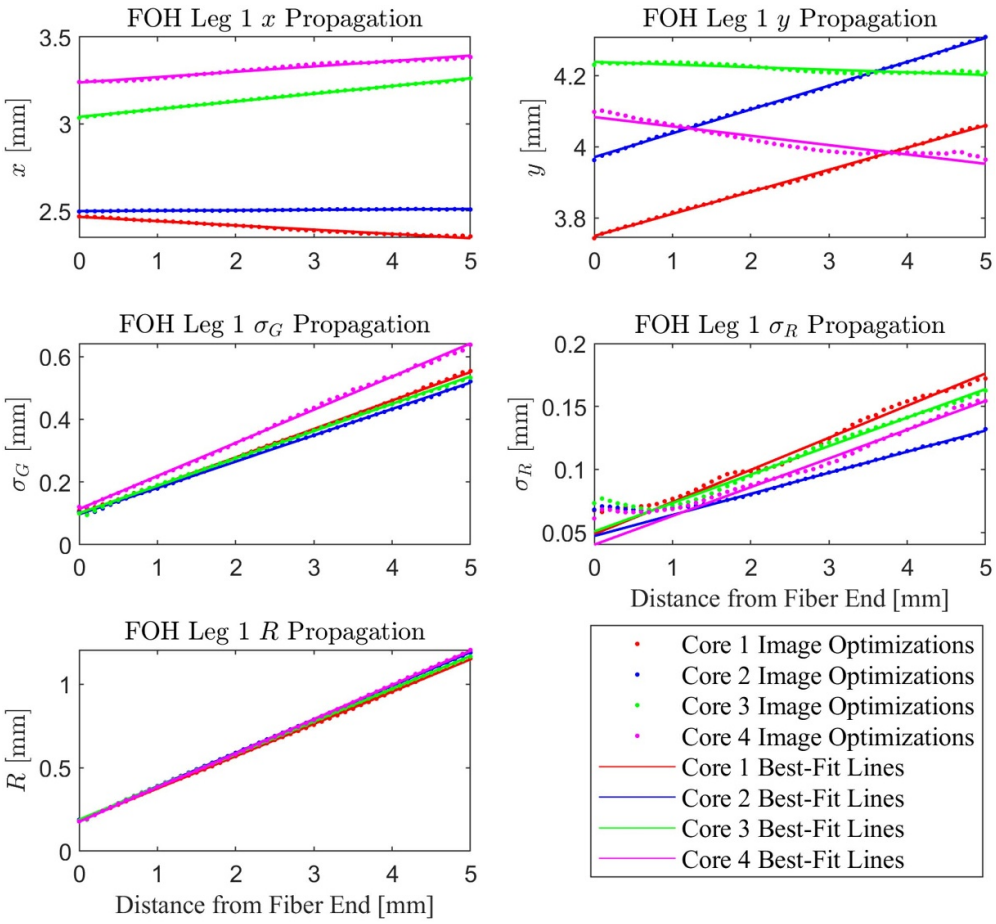

Figure 7. Gaussian parameters x, y, σ_{G}, σ_{R}, R plotted with linear fits. Note that '0' on the horizontal axis refers to 1.3 mm from the FOH output in real space, which is the distance of the closest WinCam image.

deviations since the Gaussian distribution of ray directions, further discussed in section 2.4, accounts for the beam waist characteristics. The change in the beam center, $[x, y]$, over distance allows the launch angle of a beam from a single core to be found. The change in R is the angle at which the Gaussian ring radius expands and is not the same as its divergence angle, which describes the increasing thickness of the ring.

Observing the propagation of the parameters in figure 7, x, y, σ_{G}, and R all exhibit excellent linear fits. The nonlinear near-field behavior displayed by σ_{R} is assumed to arise from convolution with the main Gaussian, as it exhibits the expected linear behavior in the far field. The Gaussian amplitudes both decrease with distance according to the inverse square law. Substituting the least squares result for each of the 29 parameters into equation (4) gives an expression for the light profile as a function of distance, d, forming a mathematical model of the FOH light output, $f_{\mathrm{beam}}(d)$.

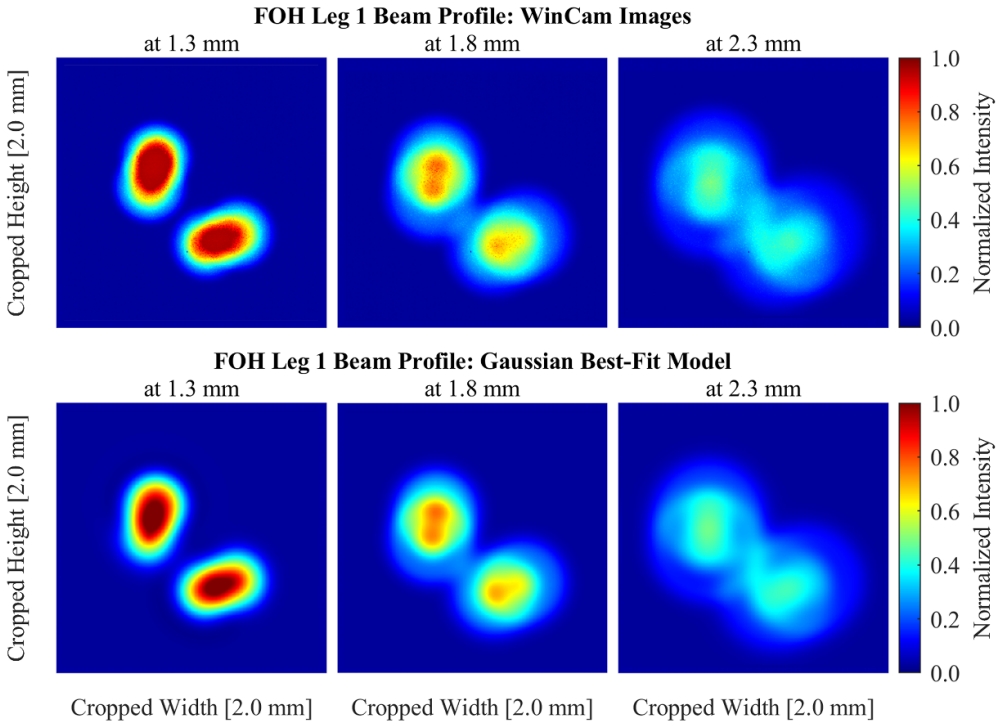

Figure 8. Comparison of FOH prototype leg 1 WinCam images (top row) at 1.3 mm, 1.8 mm, and 2.3 mm to corresponding beam profiles generated by the MATLAB best-fit model (bottom row).

2.3. FOH model results

To evaluate the accuracy of the model, WinCam images are compared to the beam profile generated by equation (4) at corresponding distances. Taking the relative root sum of squares error (RRSSE), given by

$$\mathrm{RRSSE} = \sqrt{\frac{\sum_{X,Y}\left(f_{\mathrm{beam}}(X,Y) - W(X,Y)\right)^2}{\sum_{X,Y} W(X,Y)^2}} \tag{6}$$

gives the error in the modeled beam profile for a particular distance. Taking the mean error across all distances yields a percent RRSSE of $5.2\% \pm 1.3\%$ for the FOH prototype leg 1 best-fit model. The models for legs 2, 3, and 4 yield similar RRSSE results, with mean errors of $5.6\% \pm 1.5\%$, $5.3\% \pm 1.9\%$, and $5.4\% \pm 1.8\%$, respectively. Applying the RRSSE to each individually optimized parameter set for an image also quantifies how well equation (5) was minimized. The mean percent RRSSE for the individual optimization of each distance step is $3.6\% \pm 0.3\%$, which was constant across all four legs. This indicates that the data used in the least-squares fits closely resembles the real beam profile parameters. The equation (4) model of the beam profile for leg 1 of the FOH prototype is shown in figure 8 compared to corresponding WinCam images.

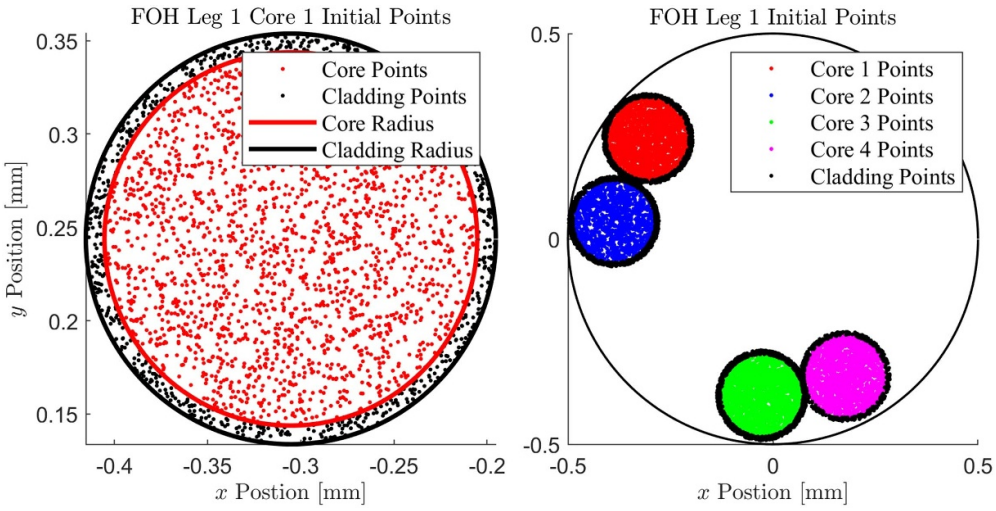

Figure 9. Left: example of random uniform distribution of points for core 1 of leg 1. Right: example of entire initial point distribution for leg 1, with each core overlaid on entire FOH tip face.

2.4. Gaussian ray distribution

Each of the Gaussian parameters with a linear fit $(x, y, R, \sigma_G, \sigma_R)$ defines an angular component needed to generate a ray distribution that models the FOH light output. The change in the center of a core's beam, $[x, y]$, with distance corresponds to the launch angle out of the FOH tip in both the x and y directions, given by

$$\begin{aligned} \theta_{\text{launch},x} &= \arctan(m_x) \\ \theta_{\text{launch},y} &= \arctan(m_y) \end{aligned} \tag{7}$$

where m_x and m_y are the slope of the best-fit lines for x and y in figure 7, respectively. The launch angle is measured relative to the normal to the tip face (z-axis). The expansion angle of the Gaussian ring and divergence half-angles of the 1σ beam width for the main Gaussian peak and Gaussian ring are calculated in the same way as equation (7) with their respective linear fit slopes from figure 7.

Collectively, these angles describe the angular distribution of light rays emitted from a single FOH core. Extending this model to all four illuminated cores produces a complete ray model of the FOH light output for a given leg.

The FOH output resembles a top-hat profile in the near-field since the flux is roughly uniform across the fiber tip surface, likely due to a modal superposition. In the far-field, however, the FOH output resembles a Gaussian profile, allowing for its propagation to be modeled with Gaussian parameters. Thus, the ray model will consist of direction vectors (rays) with a random Gaussian angular component emitted from a uniform point distribution. Initial points are distributed on the four core surface geometries for a given leg, as shown in figure 9. The power of the light emitted from each core is not equal; integrating equation (3) for each core gives the respective output powers. Integrating each main Gaussian (equation (1)) and Gaussian ring (equation (2)) component in equation (4) gives the power in each respective part of the beam, and the total power when summed. If N total rays are simulated, the number of rays emitted

from each core is given by the core's fractional power relative to the total beam power. It is assumed that the ring is caused by a cladding mode, where light enters the cladding ring and exits in the Gaussian ring shape. For each core, a uniform point distribution is generated over the 100 μm-radius circle and a separate set of points are uniformly distributed within the 10 μm-thick cladding annulus, with the number of points proportional to the respective power fractions.

To generate the Gaussian ray distribution, each initial point is assigned a random ray direction. Rays in the main Gaussian are generated by applying rotations to a ray traveling straight in the z direction. These rotations account for the launch angles and include a randomized Gaussian component to model divergence. Rays in the Gaussian ring undergo the same rotations, but their initial direction is tilted by the ring's expansion angle, θ_{R}, based on the initial point's azimuth. From an initial point, the ray direction vector is computed by

$$\overrightarrow{r} = \mathbf{R}_{\alpha}\mathbf{R}_{\beta}\overrightarrow{r}_0 = \begin{bmatrix} \cos\alpha & 0 & \sin\alpha \\ 0 & 1 & 0 \\ -\sin\alpha & 0 & \cos\alpha \end{bmatrix} \begin{bmatrix} 1 & 0 & 0 \\ 0 & \cos\beta & -\sin\beta \\ 0 & \sin\beta & \cos\beta \end{bmatrix} \begin{bmatrix} \sin\theta_{\mathrm{R}}\cos\phi \\ \sin\theta_{\mathrm{R}}\sin\phi \\ \cos\theta_{\mathrm{R}} \end{bmatrix} \tag{8}$$

where:

$\alpha = \theta_{\mathrm{launch},x} + \mathcal{N}(0,\theta_\sigma)$ is the x-direction contribution
$\beta = \theta_{\mathrm{launch},y} + \mathcal{N}(0,\theta_\sigma)$ is the y-direction contribution
ϕ is the azimuthal angle of the initial point

For the main Gaussian, $\theta_{\mathrm{R}} = 0$, so $\overrightarrow{r}_0 = [0 \quad 0 \quad 1]^T$. Applying equation (8) to all N initial points produces N 3-dimensional rays that characterize the FOH light output for input into a ray tracing simulation of the OFT geometry.

3. OFT ray tracing simulation

To produce a ray model of the OFT light output, the FOH ray distribution described in section 2.4 was propagated through the OFT geometry using COMSOL Multiphysics' Ray Optics Module. This module calculates the ray trajectories and reflections within the OFT to produce the direction vector for each ray as it exits the OFT. These ray directions, along with a power value associated with each ray, model the light injected into the GRS.

The process for characterizing the measured OFT light output followed a procedure similar to that described in section 2.1, where WinCam images were collected and compared to the beam profiles generated by the ray model.

3.1. Experimental characterization of OFT light output

Since UF is not in possession of the exact LISA OFT shown in figure 3(b), a similar optical vacuum feedthrough was used for validation of the ray model. An Accu-Glass bolt style high vacuum optical feedthrough with internal core and cladding characteristics identical to those of the LISA OFT, although longer (10.43 cm), was chosen to validate the ray model, and is referred to as the validation OFT (V-OFT). The V-OFT has a 1 mm diameter silica core with 0.1 mm F-doped silica cladding with refractive indices of $n_{\mathrm{core}} = 1.504$ and $n_{\mathrm{cladding}} = 1.488$.

The FOH prototype and V-OFT were coupled via a standard SMA905 fiber optic connector, which has a 0.3 mm gap between the fiber tip surfaces. The V-OFT and its test setup are shown in figure 10. To characterize the measured light output of the V-OFT, WinCam images were

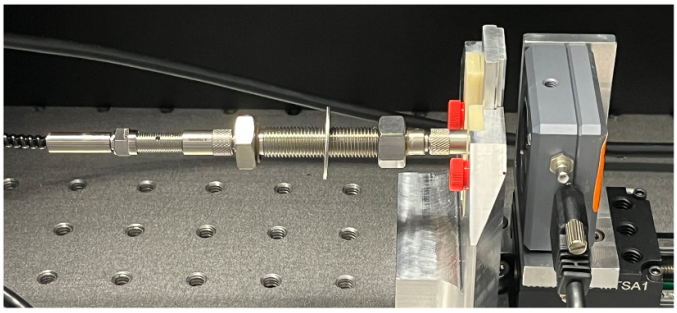

Figure 10. Image of V-OFT directed into WinCam on optical bench test setup.

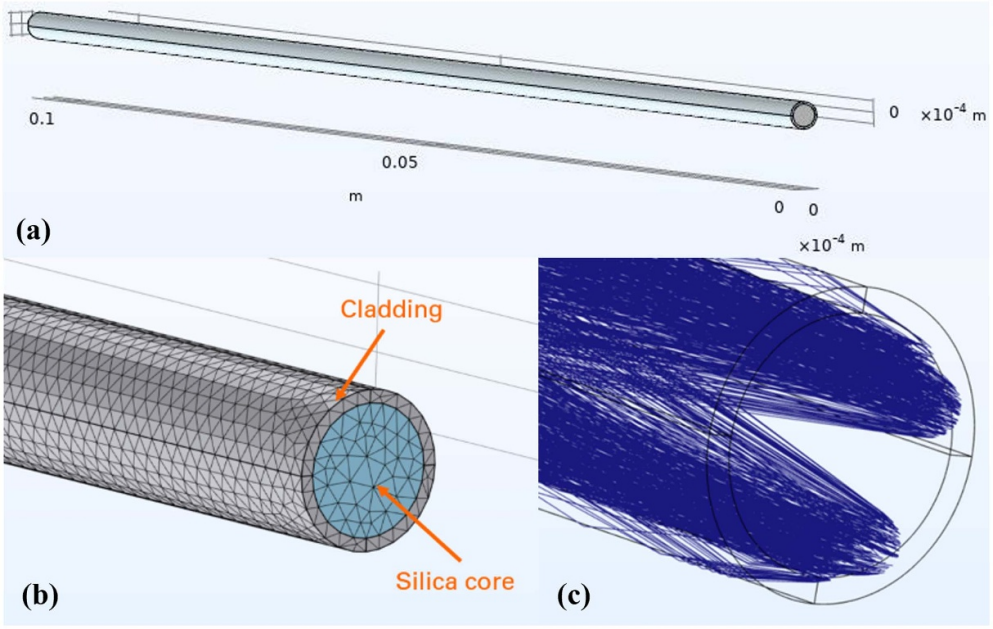

Figure 11. (a) Full 10.4 cm length of V-OFT internal structure geometry in COMSOL. (b) Close-up view of core and cladding in COMSOL model. (c) Ray distribution injection of FOH leg 1 model (1000 rays pictured).

captured at six distances given in mm: 1.3, 2.3, 3.3, 7.3, 8.3, and 9.3 from the V-OFT tip. The imaging procedure was repeated with each FOH leg configuration coupled to the V-OFT input. The V-OFT power output was also measured for each FOH leg input.

3.2. COMSOL ray tracing simulation

The V-OFT internal geometry was built in the COMSOL Multiphysics Ray Optics Module. The ray distribution for each FOH leg, described in section 2.4, was imported into COMSOL and allowed to propagate through the model. With the input face of the V-OFT at 0.0 mm, the starting point of the rays on the z-axis was set to -0.3 mm to account for the SMA connector gap. The geometry and ray injection can be seen in figure 11.

Within COMSOL, the input ray distribution was assigned a power that was uniformly distributed across all rays. The total power was assigned as the measured FOH output power for that respective leg. For example, the FOH leg 1 output power was measured at 865 nW via power meter, so this was assigned to the leg 1 rays in COMSOL. The output of the COMSOL simulation is an $N \times 4$ text file containing each ray's $[x, y, z]$ position at specified slices along the z axis, as well as an associated power value in the fourth column. These slices were set to match the WinCam image distances as well as the fiber surfaces for power transmission analysis. The $N \times 4$ text file was analyzed in MATLAB and used to create a 2-dimensional histogram of the ray power distribution, with each bin size matching the WinCam image pixel size of 5.5 μm $\times$ 5.5 μm. This process allows for direct comparison of the simulated beam and the measured WinCam beam profiles.

All simulations were run with input ray distributions of $N = 10^6$, $N = 5 \times 10^5$, and $N = 10^5$ as simulations with $N > 10^6$ caused COMSOL to time out. The COMSOL outputs for each N count were combined during analysis in MATLAB to reduce shot noise in the generated 2-dimensional power histograms.

4. Simulation results

To validate the final ray model, the simulated V-OFT beam was compared to measured beam profiles, as was done for the FOH model. Three important metrics were chosen to validate the simulated light output:

1. Power transmission of V-OFT
2. Divergence angles of radii enclosing 50% and 95% of beam power
3. RRSSE between simulated beam profiles and WinCam images

The results for all four leg configurations of the FOH prototype are presented below in tables. Figures are presented for only legs 1 and 3 to show both extremes of the illuminated core patterns, where the cores are all peripheral in leg 1 and mostly central in leg 3.

4.1. Power output

For each leg, the power outputs of the FOH and the FOH-coupled V-OFT were measured for each FOH prototype leg. The measured FOH power for each leg was assigned to the ray distribution input in COMSOL, scaling each leg's modeled power. The power of the ray distribution at the end of the V-OFT model was calculated by summing the power of each ray at the V-OFT output surface, which was compared to the measured output power of the V-OFT for each FOH leg.

The measured power values and simulation results are presented in table 1 for all four leg configurations. The simulated power transmission closely matches the measurements, with relative percent error for all four legs falling under 3%. The uncertainty of the simulated power outputs is higher for legs 1 and 2, which may be due to the peripheral position of the illuminated cores for those legs; there may be more variation in power loss at the FOH-OFT coupling interface. Overall, the results indicate that the simulation accurately reproduces the experimentally observed power for each leg configuration.

Table 1. Power outputs of FOH and V-OFT for each leg with simulation results.

Leg	FOH output (nW)	V-OFT output (nW)	Simulated V-OFT output (nW)	Ray model % error
1	$865 \pm 61^{a}(6.2^{b})$	$767 \pm 54^{a}(7.6^{b})$	747 ± 28	2.6%
2	$1030 \pm 72^{a}(8.7^{b})$	$910 \pm 64^{a}(2.6^{b})$	890 ± 27	2.2%
3	$1050 \pm 74^{a}(6.7^{b})$	$931 \pm 65^{a}(1.3^{b})$	918 ± 16	1.4%
4	$895 \pm 63^{a}(2.5^{b})$	$778 \pm 54^{a}(9.9^{b})$	784 ± 11	0.8%

[a] $\pm 7\%$ measurement uncertainty of Thorlabs S120VC photodiode power sensor.
[b] Uncertainty between repeated measurements.

Table 2. Beam divergence results.

Metric	Leg	Measured half-angle (°)	Simulated half-angle (°)	Ray model % error
50% Power divergence	1	7.8 ± 0.10	7.4 ± 0.11	4.5%
	2	7.6 ± 0.13	7.3 ± 0.10	3.6%
	3	8.1 ± 0.04	7.4 ± 0.07	8.1%
	4	7.7 ± 0.08	7.9 ± 0.10	3.2%
95% Power divergence	1	14.1 ± 0.08	13.8 ± 0.16	2.2%
	2	14.0 ± 0.09	13.5 ± 0.21	3.5%
	3	12.7 ± 0.09	11.7 ± 0.07	8.1%
	4	13.1 ± 0.23	12.5 ± 0.07	5.2%

4.2. Beam divergence

The chosen metrics for evaluating the beam divergence are the divergence half-angles of the radii enclosing 50% and 95% of the beam power, i.e. the radius such that the given percentage of the beam's total power is within that radius at a given distance. These metrics, rather than the full width at half maximum or Gaussian beam diameter defined by an intensity drop of $1/e^2$, were chosen due to their presence in LISA requirements and LPF heritage. The 50% and 95% power radii were found for each WinCam image and plotted against the distance. As in equation (7), the inverse tangent of the slope of the linear fit gives the far-field divergence half-angle. The same is done for the simulated beam by generating a 2-dimensional power histogram from the ray positions and power values computed by COMSOL. A power histogram was generated for each image distance between 0.0 mm and 9.3 mm from the V-OFT surface. The power histograms were used to find the 50% and 95% power radii, and then the divergence angles of the simulated beam.

The measured and simulated 50% and 95% divergence half-angles are presented for all four legs in table 2. The 95% power divergence half-angles are slightly greater than the expected maximum acceptance half-angle of 12.6°, suggesting agreement between the model and theoretical constraints. The simulated 50% and 95% divergence angles trend slightly lower than the measured values, indicating a possible underestimation of scattering or aberrations in the geometrical optics simulation.

The plotted power radii for legs 1 and 3 are shown in figure 12. The deviation between the two legs' 95% power divergence can be seen, where leg 1 (with peripheral cores) has a larger angular spread. Additionally, leg 3 (with mostly central cores) has a smaller 50% power radii

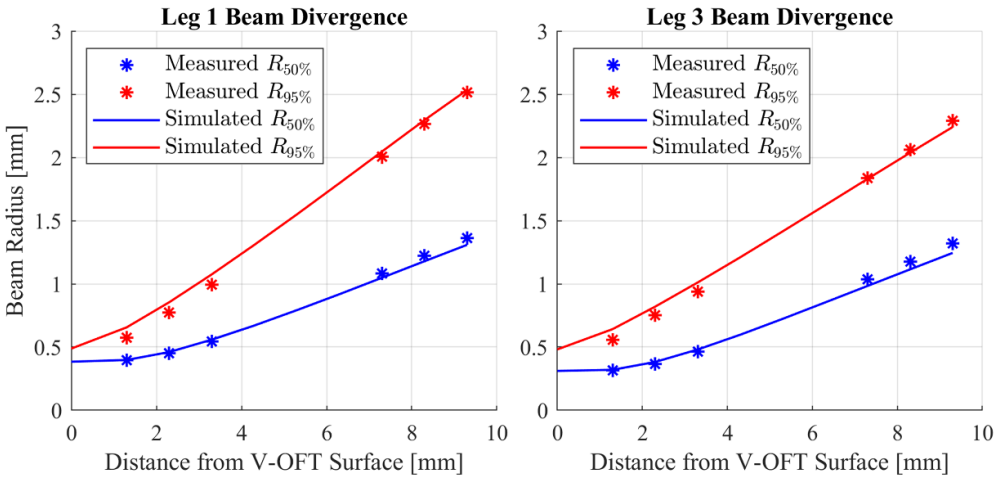

Figure 12. V-OFT beam divergence for FOH prototype legs 1 and 3. $R_{50\%}$ and $R_{95\%}$ designate the 50% and 95% power radii, respectively.

in the near field. Though there is consistent underestimation of the divergence half-angles, the measured differences between each leg are captured by the ray model.

4.3. Beam profile

The simulated beam profiles are assessed both qualitatively and quantitatively. Qualitative evaluation is based on visual comparison, while quantitative evaluation is performed using the RRSSE as defined in equation (6). The power histograms used to determine the divergence angles also serve to evaluate the accuracy of the simulated V-OFT beam, with RRSSE values calculated by comparing the simulated profiles to the corresponding WinCam images at matching distances. The leg 1 and leg 3 power histograms 1.3 mm from the V-OFT surface are shown in figure 13. The shot noise in the simulated beam profiles arises from the computationally limited low N counts of 10^5–10^6, relative to the trillions of photons that generate the WinCam images. While this noise introduces large deviations between adjacent pixels, which makes the direct comparison of measured and simulated beam profiles via the RRSSE somewhat impractical, it still serves as a useful quantitative measure to assess the performance of the ray model.

The RRSSE was calculated at each of the six WinCam image distances for all four FOH legs. Taking the mean across the distance sweep yields: 16.1% $\pm$ 2.17% for leg 1, 18.1% $\pm$ 1.20% for leg 2, 16.8% $\pm$ 1.80% for leg 3, and 10.5% $\pm$ 0.65% for leg 4.

Qualitatively comparing the beam profiles, figure 13 demonstrates that the ray model accurately reproduces the observed differences between a peripheral core pattern and a central core pattern through legs 1 and 3 in the FOH prototype. The peripheral core pattern of leg 1 produces a ring of elevated intensity around the outer edge of the V-OFT in the beam profile. Leg 3, with a more central core pattern, produces a beam profile with the power centralized near the center of the beam. Additionally, the ray model accurately reproduces the lobes in the center of the beam profile for both legs shown. The simulated beam profiles appear to have a larger angular spread, i.e. the dark blue zero-power regions appear smaller or nonexistent in

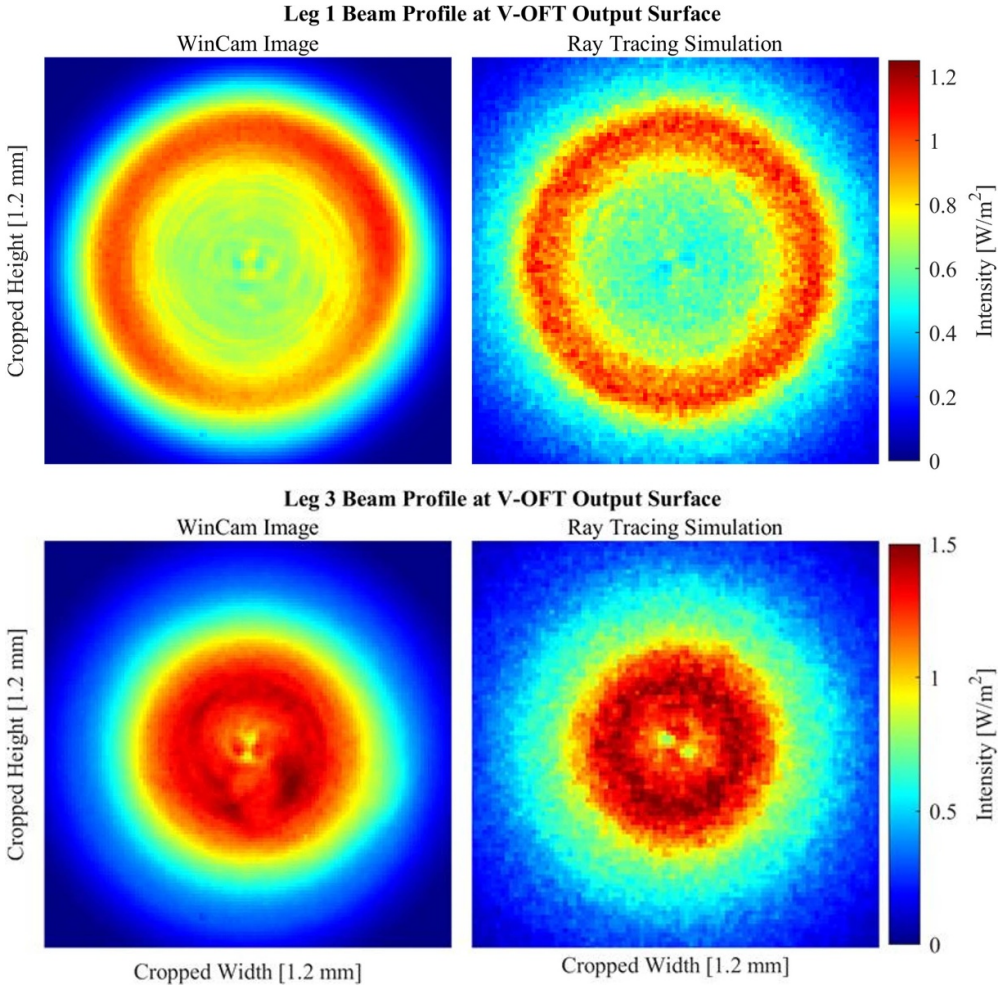

Figure 13. Measured and simulated V-OFT beam profile 1.3 mm from V-OFT tip for FOH prototype legs 1 and 3.

the simulated profile, while present in the WinCam images. This is also observed in figure 12, where the simulated 95% power radii track just above the measured values in the near field.

The objective of the FOH-OFT simulation was to develop a ray model for each leg such that the differences between the legs' light profiles are accurately characterized in a ray distribution to study the effects of the redundant LISA FOH design. The presented model achieves this objective and will be used as an input for the aforementioned photoelectric charge management simulation.

5. Conclusions

This paper presents a ray model that accurately characterizes the UV light beam injected into the LISA GRS for each of the four leg configurations in the new LISA FOH design. The LISA FOH and OFT light outputs are characterized and the development process of the ray model

is detailed. The ray model was developed to generate a UV light beam input for a photoelectric charge management simulation, which will investigate the effects of the new, redundant LISA FOH design on the discharge efficiency of the CMS. The ray model was validated using a vacuum optical feedthrough similar to the LISA OFT. The model accurately described the differences between the FOH legs and their respective core patterns. The ray model simulated the OFT power output within 0.8%–2.6% of the measured values. Additionally, the ray model simulated the 50% and 95% power divergence half-angles within 2.2%–8.1% of the experimental values obtained from WinCam images of the beam. Finally, the simulated beam profiles of the ray model accurately represented the corresponding WinCam images and captured the resultant beam differences dependent on the FOH leg configuration.

This ray model accurately characterizes the differences between the LISA FOH legs and has been sufficiently validated such that it will be used to generate ray distributions for the LISA photoelectric charge management simulation. The simulation results presented in section 4 were for the light output of the on-hand OFT, or V-OFT, which was used to validate the model. For the photoelectric charge management simulation, the ray distribution must be representative of the LISA OFT light output. The LISA OFT is nearly identical to the V-OFT used for validation; it has the same internal structure and optical properties, but is 3.7 cm shorter. To generate a ray model of the LISA OFT light output, the geometry in COMSOL will simply need to be adjusted and all simulations rerun with the updated geometry. Following this change, the presented model will be able to accurately define a ray distribution of the LISA OFT light output for further study.

Data availability statement

The data cannot be made publicly available upon publication because no suitable repository exists for hosting data in this field of study. The data that support the findings of this study are available upon reasonable request from the authors.

Acknowledgments

We would like to acknowledge the funding source that made this research possible, the NASA LISA Charge Management Device Engineering Development Contract 80GSFC21C0012.

ORCID iDs

Corey J Richardson 0009-0004-9637-6156
Peter J Wass 0000-0002-2945-399X

References

[1] Abbott B P *et al* (LIGO Scientific Collaboration and Virgo Collaboration) 2016 *Phys. Rev. Lett.* **116** 061102
[2] Abbott B P *et al* (LIGO Scientific Collaboration and Virgo Collaboration) 2017 *Phys. Rev. Lett.* **119** 161101
[3] The eLISA Consortium 2013 The gravitational Universe (arXiv:1305.5720)
[4] Colpi M *et al* 2024 LISA definition study report (arXiv:2402.07571)
[5] Araújo H M, Wass P, Shaul D, Rochester G and Sumner T J 2005 *Astropart. Phys.* **22** 451–69
[6] Jafry Y, Sumner T J and Buchanan S 1996 *Class. Quantum Grav.* **13** A97–A106
[7] Armano M *et al* 2023 *Phys. Rev. D* **107** 062007

[8] Wass P 2007 The charged particle space environment as a noise source for LISA and LISA pathfinder *PhD Thesis* Imperial College London
[9] Reigber C, Lühr H and Schwintzer P 2002 *Adv. Space Res.* **30** 129–34
[10] Tapley B D, Bettadpur S, Watkins M and Reigber C 2004 *Geophys. Res. Lett.* **31** L09607
[11] Kornfeld R P, Arnold B W, Gross M A, Dahya N T, Klipstein W M, Gath P F and Bettadpur S 2019 *J. Spacecr. Rockets* **56** 931–51
[12] Everitt C W F *et al* 2015 *Class. Quantum Grav.* **32** 224001
[13] Wass P, Hollington D, Sumner T J, Yang F and Pfeil M 2019 *Rev. Sci. Instrum.* **90** 064501
[14] Wang S, Saraf S, Lipa J, Yadav D and Buchman S 2022 *Class. Quantum Grav.* **39** 195008
[15] Letson B, Barke S, Wass P, Mueller G, Ren F, Pearton S and Conklin J 2023 *J. Vac. Sci. Technol. A* **41** 013202
[16] Buchman S, Al Saud T S M, Alfauwaz A, Byer R I, Klupar P, Lipa J, Lui C Y, Saraf S, Wang S and Worden P 2022 *Class. Quantum Grav.* **40** 025010
[17] Kenyon S P, Apple S, Siu J, Wass P J and Conklin J W 2025 *Class. Quantum Grav.* **42** 055013
[18] Armano M *et al* (LISA Pathfinder Collaboration) 2018 *Phys. Rev. D* **98** 062001
[19] Yan Y, Wang G, Sun W, Luo A, Ma Z, Li J and Wang S 2016 *Mon. Not. R. Astron. Soc.* **466** 1669–87
[20] Armano M *et al* 2015 *J. Phys.: Conf. Ser.* **610** 012005
[21] Buchman S, Quinn T, Keiser G M and Gill D 1995 *Rev. Sci. Instrum.* **66** 120–9
[22] Hollington D 2011 The charge management system for LISA and LISA pathfinder *PhD Thesis* Imperial College London
[23] CVI Melles Griot 2009 CVI technical guide: gaussian beam optics (available at: www.idexot.com/techguide-online)